

Research Article

Study of the Mechanical Properties of a Nanostructured Surface Layer on 316L Stainless Steel

F. C. Lang,¹ Y. M. Xing,¹ J. Zhu,² and Y. R. Zhao³

¹School of Science, Inner Mongolia University of Technology, Hohhot 010051, China

²The Sixth Academy of China Aerospace Science & Industry Corporation, Hohhot 010050, China

³School of Civil Engineering, Inner Mongolia University of Technology, Hohhot 010051, China

Correspondence should be addressed to Y. M. Xing; xym@imut.edu.cn

Received 11 October 2015; Accepted 5 May 2016

Academic Editor: Massimiliano Barletta

Copyright © 2016 F. C. Lang et al. This is an open access article distributed under the Creative Commons Attribution License, which permits unrestricted use, distribution, and reproduction in any medium, provided the original work is properly cited.

A nanostructured surface layer (NSSL) was generated on a 316L stainless steel plate through surface nanocrystallization (SNC). The grains of the surface layer were refined to nanoscale after SNC treatment. Moreover, the microstructure and mechanical properties of NSSL were analyzed with a transmission electron microscope (TEM) and scanning electron microscope (SEM), through nanoindentation, and through reverse analysis of finite element method (FEM). TEM results showed that the grains in the NSSL measured 8 nm. In addition, these nanocrystalline grains took the form of random crystallographic orientation and were roughly equiaxed in shape. In situ SEM observations of the tensile process confirmed that the motions of the dislocations were determined from within the material and that the motions were blocked by the NSSL, thus improving overall yielding stress. Meanwhile, the nanohardness and the elastic modulus of the NSSL, as well as those of the matrix, were obtained with nanoindentation technology. The reverse analysis of FEM was conducted with MARC software, and the process of nanoindentation on the NSSL and the matrix was simulated. The plastic mechanical properties of NSSL can be derived from the simulation by comparing the results of the simulation and of actual nanoindentation.

1. Introduction

Nanocrystalline materials [1, 2] exhibit novel properties, unlike their coarse-grained polycrystalline counterparts. The majority of the failures in engineering materials are sensitive to the structure and properties of the material surface, and most such failures are initiated at the surface. Therefore, optimizing surface structure and properties may enhance the global behavior of materials. Surface nanocrystallization (SNC) [3] can improve the overall properties and behaviors of materials. Surfaces are modified by generating a nanostructured surface layer (NSSL). This layer is regarded as a well-known surface technology. Most surface treatments can be used for SNC, including surface mechanical attrition treatment (SMAT) [4–7], high-energy shot peening [8], surface mechanical rolling treatment [9], and ultrasonic shot peening (USSP) [10–12]. Among these treatments, USSP is considered a promising process that can rapidly and

effectively realize SNC. Researchers [13–17] have conducted simple theoretical analyses of the SNC process to determine the residual stresses and the plastic deformations in the initially affected layers of the shot peened part. In [10], the mechanism of nanocrystallization was analyzed in terms of deformation behavior and the transmission electron microscope (TEM) observations of the microstructural evolution of 316L stainless steel after SNC treatment. The residual stress on this steel as induced by ultrasonic shot peening was studied using the moiré interferometry method and the finite element method (FEM) [18, 19]. The thermal stability of the structure of 316L stainless steel after SMAT was examined in [20]. The wear and friction properties of low-carbon steel were significantly improved by USSP [21]. In addition, the 316L stainless steel that was subjected to the SMAT technique also exhibited the maximum yield strength of 1450 MPa, which is approximately six times higher than that of the coarse-grained sample [8]. However, the effect of USSP on surface

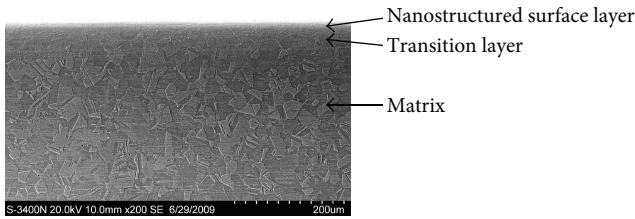


FIGURE 1: SEM image of the sample after SNC treatment with NSSL.

properties (e.g., nanohardness, elastic modulus, and plastic mechanical properties) of 316L stainless steel has not been investigated in detail.

In the current study, 316L stainless steel is selected for USSP treatment. An NSSL that is approximately $10\ \mu\text{m}$ thick is generated on such a plate. The microstructural and mechanical properties of NSSL are analyzed using TEM, a scanning electron microscope (SEM), and nanoindentation technology. Furthermore, the process of nanoindentation is numerically simulated with the finite element software (MSC MARC). The plastic mechanical properties of the NSSL are derived from the simulation process.

2. Experiment Procedure

2.1. Sample Preparation. The material used in this work is a 316L stainless steel plate that is 1 mm thick. Its chemical composition includes (mass %) 0.019 C, 17.07 Cr, 11.95 Ni, 2.04 Mo, 1.68 Mn, 0.04 Cu, and 0.007 S. The sample was treated using USSP. The cross-sectional SEM image is shown in Figure 1.

The principle of the USSP is based on the vibration of spherical shots obtained through high-powered ultrasound. Given the high frequency of the system, the entire surface of the component for treatment is peened with a high number of impacts in a short period. Each instance of peening the ball to the surface initiates plastic deformation on the surface layer of the treated sample. As a result, repeated multidirectional peening onto the sample surface layer at high strain rates results in a severe plastic deformation that refines the microstructure of the surface layer of the sample to nanoscale. The transition layer is approximately $90\ \mu\text{m}$ thick and is formed underneath the NSSL during the USSP processing. The interfaces of these layers are indistinct. In this study, the main parameters of the USSP process are as follows: the vibration frequency of the chamber driven by an ultrasonic generator is 20 KHz, shot diameter is 2 mm, and processing duration is 960 s.

2.2. Experimental Method. In order to study the microstructure of the 316L stainless steel after USSP treatment, observations were made using a JEM-2010 TEM with an operating voltage of 200 KV. The TEM samples were prepared by mechanically polishing to thickness of about $30\ \mu\text{m}$ then by dimple grinding down to about $10\ \mu\text{m}$ thickness. Further thinning to reach a thickness of electron transparency was carried out using ion beam milling.

In situ SEM observation of the sample with a unilateral NSSL under axial tension was made using an S-3400N field SEM with a tensile stage. This microscope was manufactured by Deben UK Ltd. The 316L samples treated for in situ tensile tests were prepared as follows: first, the unilateral NSSL was removed through mechanical polishing to generate tensile samples with a side composed of NSSL. This process highlights the effects of NSSL on tensile properties. Second, a dog bone-shaped tensile specimen was cut by electrodischarging and followed by mechanical polishing. The final 1 mm thick tensile sample had a gauge length of 4 mm and a cross-sectional area of $1\ \text{mm} \times 1\ \text{mm}$.

The micromechanical properties of the NSSL were measured by Agilent Nano Indenter G200 with a diamond Berkovich indenter [22, 23]. The treated 316L stainless steel plate was cut into 20 mm long samples. The sample was embedded with Bakelite powder, and the test was conducted on the cross section. The indented sample was mechanically polished to a mirror with $0.5\ \mu\text{m}$ diamond polishing paste. To measure hardness and elastic modulus as function of the depth to the top surface, nanoindentation tests were conducted. All of the tests were performed on the cross sections of the treated sample with depth control. When the effect of depth on the size of the indentation is considered, the maximum indentation depth is approximately 200 nm. Nine equal space straight lines parallel to the surface were selected from along the cross section. Ten experimental tests were performed along each line, and the distance between the nearby lines is $20\ \mu\text{m}$.

2.3. Experimental Results and Discussion

2.3.1. TEM Observation. Figure 2 depicts the TEM results for the top NSSL at the amplifications of 200 K and 1.2 M. The microstructure of the NSSL is characterized by uniformly distributed nanoscale grains measuring approximately 8 nm. The corresponding electron diffraction pattern indicates that the microstructure of NSSL belongs to martensite phase, with a random orientation and a roughly equiaxed shape. From the higher magnification image, the high density of stacking faults induced by plastic deformation can be observed within the grain.

2.3.2. In Situ SEM Study. Figure 3 displays the cross-sectional, in situ SEM observational images obtained under different tensile stresses. Within the grains of the matrix, a few slips occur along 45° in the axial direction. However, the transition layer and the NSSL cannot be examined under a tensile stress of 380 MPa, as indicated in Figure 3(a). Plastic deformation is observed in the base material at 460 MPa, as suggested in Figure 3(b). However, the transition layer and the NSSL remain in the elastic stage. When the stress is 550 MPa, numerous slips occur at all the grains in the transition layer. Nonetheless, these slips do not extend beyond the NSSL, as shown in Figure 3(c). Given that the nanostructured grains on the surface display high stiffness and strength, the motions of the dislocation in front of the NSSL are blocked. As a result, slips cannot form entirely. The jam-packing of dislocation hardens the material. In addition,

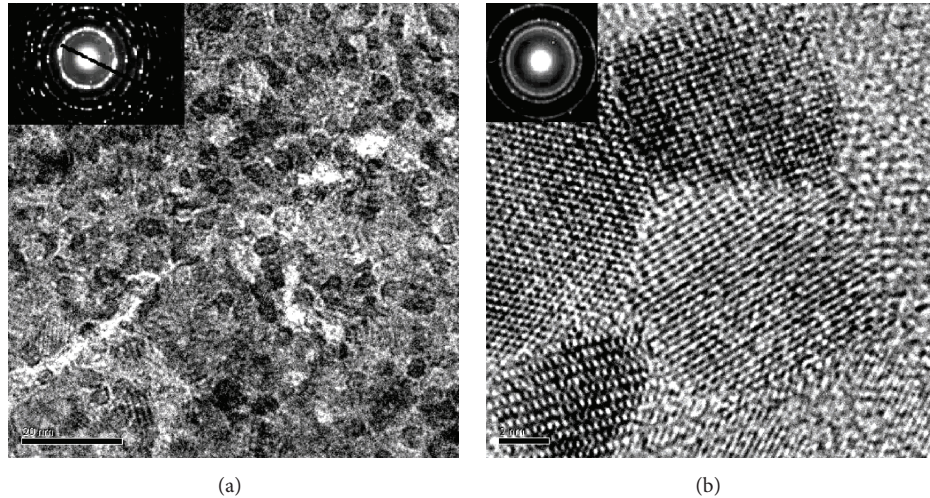


FIGURE 2: TEM images and selected area electron diffraction patterns of NSSL at different levels of magnification: (a) 200 K and (b) 1.2 M.

no nanostructured grains are found at the bottom of the sample. The dislocations are emitted and move along the slip direction. Ultimately, they move beyond the surface and form slip bands. Figure 3(d) exhibits the severe plastic deformation at all parts of the sample when the stress reaches 630 MPa. All grains are elongated and become rotational. The NSSL shared most of the load, unlike the base material. Thus, the plastic deformation is initiated in this layer.

The necking phenomenon is observed in both the top and the bottom of the sample when the tension stress is equal to 810 MPa, as indicated in Figure 3(e). The extent of necking varies. The deformation occurred at the bottom surface, where the NSSL was polished. This deformation is larger than that at the top. The cracks that were initiated at the bottom surface and propagated to the interior can be observed in the amplification region. However, crack initiation and propagation are inhibited by the fine grains near the upper surface. The residual compressive stresses introduced during SNC can effectively stop or delay these processes as well. Thus, the NSSL can effectively enhance the overall strength of the material.

Figure 4 indicates that the fracture mode was transgranular ductile. Moreover, the dimples are distributed uniformly on the fracture surface. The dimples of the matrix were considerably larger than those of the NSSL.

2.3.3. Nanoindentation Test Results. The average load-depth curves were derived on the basis of nanoindentation tests, as depicted in Figure 5. Curve 1 corresponds to the position of the NSSL and curve 9 to the matrix.

The maximum loads of all of the tested points decreased with the increase in distance to the surface under a constant maximum depth of 200 nm. The maximum load and the residual depth of the matrix were 5.52 mN and 164 nm, respectively. Those of the NSSL were 7.09 mN and 140 nm.

The hardness profiles of all points as shown in Figure 6 suggest that the average hardness of the NSSL is significantly greater than those of the others. This difference is attributed

to strain hardening, size effect, grain refinement, and the residual compressive stress in the NSSL. The elastic moduli of all of the tests are presented in Figure 7. SNC influences the elastic modulus slightly.

To determine the mechanical properties of the top surface layer (NSSL), 25 nanoindentation tests were performed on the surfaces of the topsides of the treated and untreated samples at a maximum indentation depth of 2500 nm. Figure 8 illustrates the load-depth curves of the NSSL and of the matrix. The former exhibits considerably higher strength than the latter does. The load of the NSSL reaches 653 mN at maximum depth, which is approximately thrice that of the untreated sample. Figure 9 suggests that the elastic modulus changes slightly with distance to the surface.

Figure 10 highlights the hardness obtained through nanoindentation as a function of depth for the NSSL and for the matrix. The hardness of the NSSL decreases with the increase in indentation depth. By contrast, that of the matrix follows a straight line trend that corresponds to depth. The maximum hardness of the top surface of the treated sample is approximately 8 GPa, which is roughly 2.6 times that of the matrix. The enhanced hardness on the NSSL is attributed to the presence of residual stress, as well as to the formation of nanocrystallites and of a martensite phase on the NSSL. The maximum residual stress is 531 MPa [18]. During treatment, nanometer-scale surface grains are determined through TEM. SNC yields fine, 8 nm grains near the surface. Grain size also increases from the original 40 μm with the increase in distance to the surface. The effect of refined grains on the enhancement of hardness is determined according to Hall-Petch theory, which suggests a strengthened relationship between hardness and grain size.

2.3.4. Determination of the Plastic Properties of the NSSL from Finite Element Simulation. The interfaces of the NSSL and the transition layer are indistinct, and the NSSL is only approximately 10 μm thick. As a result, separating this layer from the plane sample and determining its plastic properties

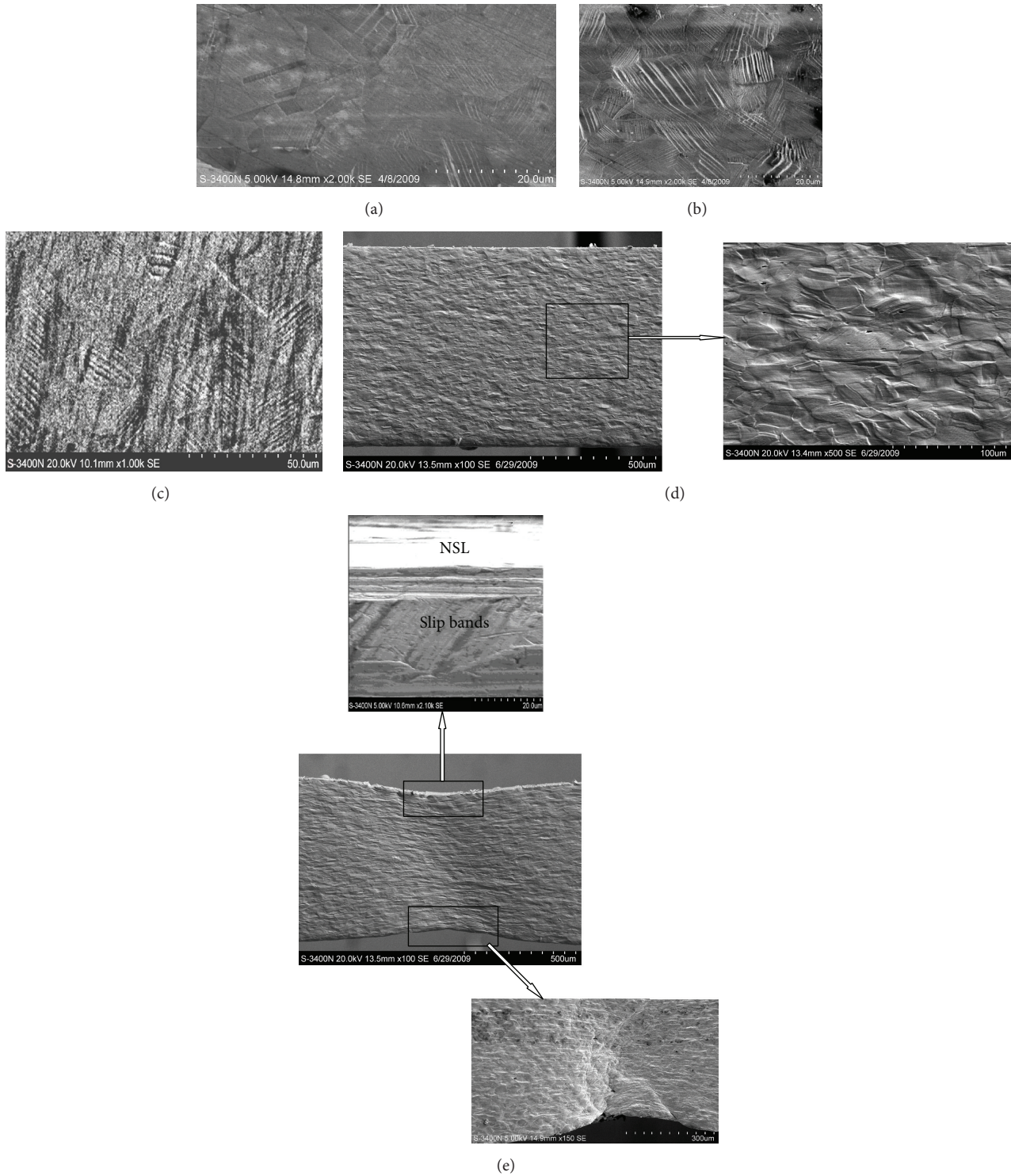


FIGURE 3: SEM images under different tensile stresses: (a) 380 MPa, (b) 460 MPa, (c) 550 MPa, (d) 630 MPa, and (e) 810 MPa.

are difficult. As presented in Figure 8, the load-depth curve of the NSSL can be described using the power law equation:

$$F = kh^2, \quad (1)$$

where F is the load; k is the curvature of the loading curve; and h is the corresponding indentation depth. Figure 11

depicts a schematic of the stress-strain curve of the power law material as expressed in the Swift equation [24]:

$$\begin{aligned} \sigma &= E\varepsilon \quad (\sigma \leq \sigma_y) \\ \sigma &= K\varepsilon^n \quad (\sigma > \sigma_y). \end{aligned} \quad (2)$$

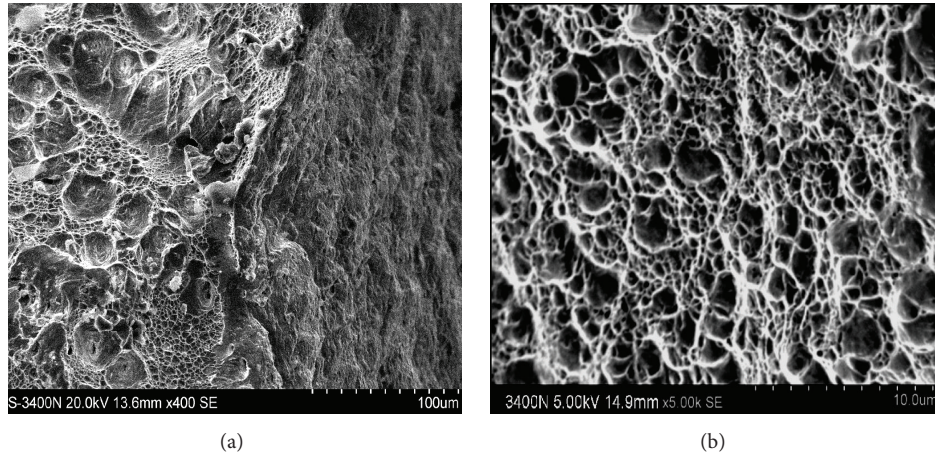


FIGURE 4: SEM fractographs: (a) on the left is the matrix and on the right is the NSSL; (b) nanostructured layer.

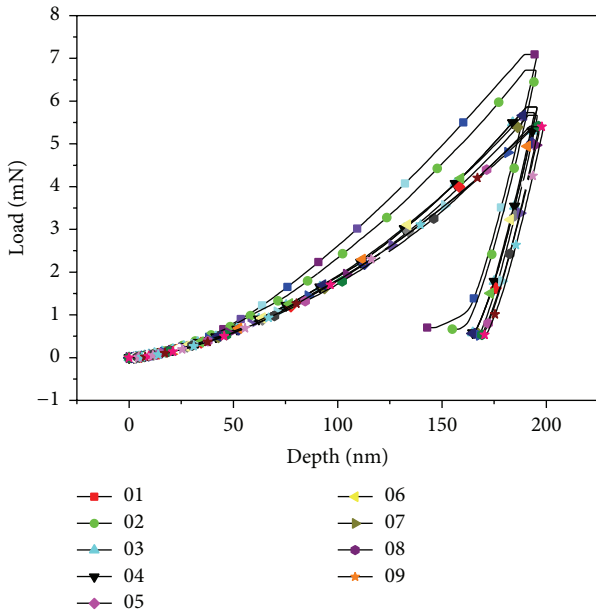


FIGURE 5: Load-depth curves at different positions.

When $\sigma > \sigma_y$, stress can also be expressed as

$$\sigma = \sigma_y \left(1 + \frac{E}{\sigma_y} \varepsilon_f \right)^n, \quad (3)$$

where ε_f is the total effective strain accumulated beyond the yield strain ε_y , and representative stress σ_r is the flow stress defined at $\varepsilon_f = \varepsilon_r$.

Dao et al. [24] also proposed a group of six dimensionless functions that relate the characteristic parameters of indentation loading-unloading curves to the mechanical properties derived from the stress-strain curves.

A function relates the ratio of the constant of Kick's law to representative stress. This law is generally used to describe

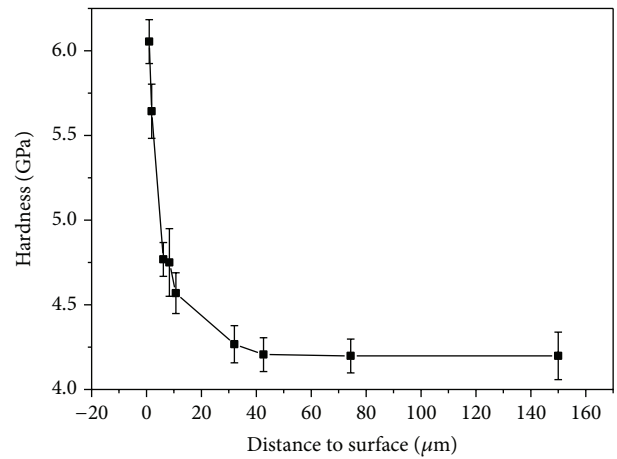


FIGURE 6: Curve of the hardness that corresponds to distance to the surface.

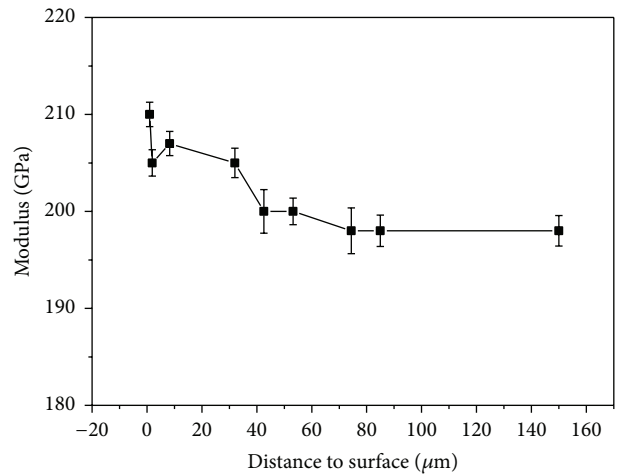


FIGURE 7: Curve of the elastic modulus that corresponds to distance to the surface.

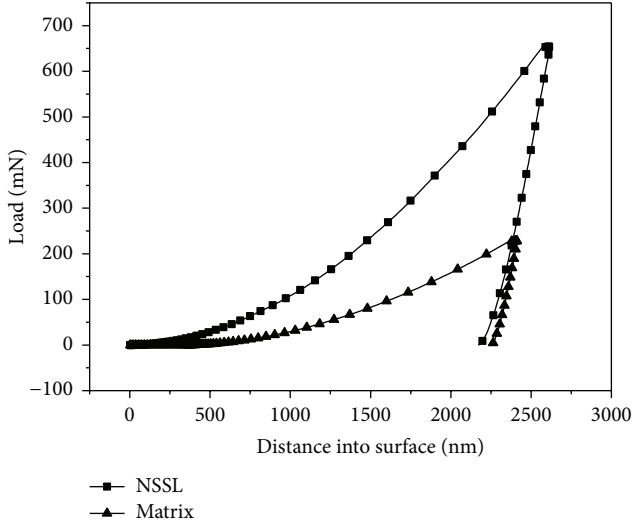


FIGURE 8: Load-depth curves of the NSSL and of the matrix.

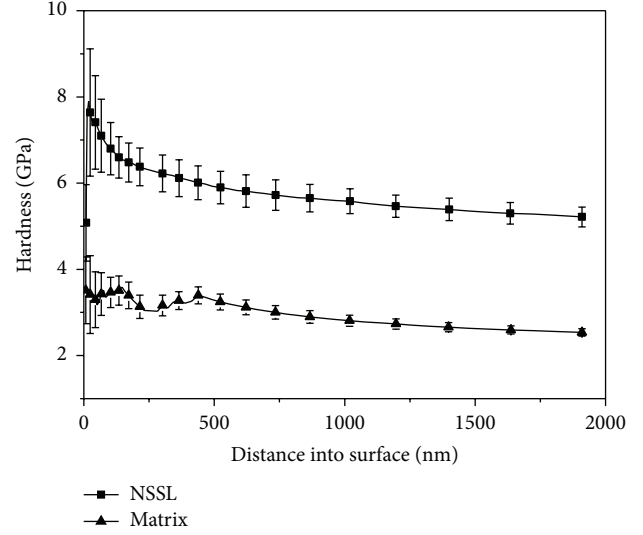


FIGURE 10: Hardness of the NSSL and of the matrix.

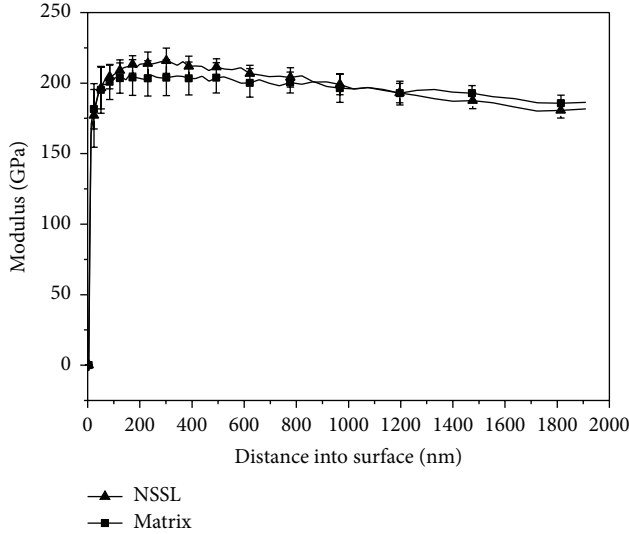


FIGURE 9: Elastic moduli of the NSSL and the matrix.

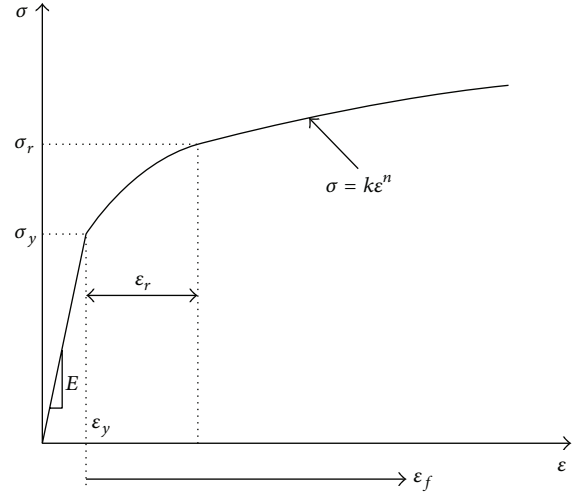


FIGURE 11: Schematic of the stress-strain relationship in power law.

the indentation-loading curve. The dimensionless function is written as

$$\frac{k}{\sigma_r} = \prod \left(\frac{E_r}{\sigma_r}, n \right), \quad (4)$$

where n is the strain-hardening exponent of the stress-strain curve. The reduced Young modulus E_r is given by

$$\frac{1}{E_r} = \frac{(1 - \nu_s^2)}{E} + \frac{(1 - \nu_i^2)}{E_i}, \quad (5)$$

where E and E_i are Young's moduli. ν_s and ν_i are the Poisson ratios of the material and of the indenter, respectively. In [24], ε_r was set 0.33, which corresponds to the representative value of plastic strain that best fits function \prod and is independent of the strain-hardening exponent n . In this study, the representative strain is assumed to be 0.033. Antunes et al.

[25] determined that the representation of the inverse of the ratios E_r/H exhibits linear behavior as a function of E_r/σ_r . The linear fitting is expressed as

$$\frac{E_r}{H} = 0.231 \left(\frac{E_r}{\sigma_r} \right) + 4.910. \quad (6)$$

The commercial software MSC.MARC was used to simulate the nanoindentation process involving the indentation of material by a rigid indenter. An ideally axisymmetric conical indenter of similar area-depth functioned as the Berkovich indenter to simplify the analysis to a two-dimensional axisymmetric problem. Therefore, an equivalent perfect conical indenter with a semiapical angle of $\theta = 70.3^\circ$ was obtained. The specimen was modeled as a deformation and meshed with 4,616 three-node triangle elements. The friction between the indenter and the deformable body presumably had a friction coefficient of 0.2 [26–28]. The elements near the region of contact were refined to improve the numerical

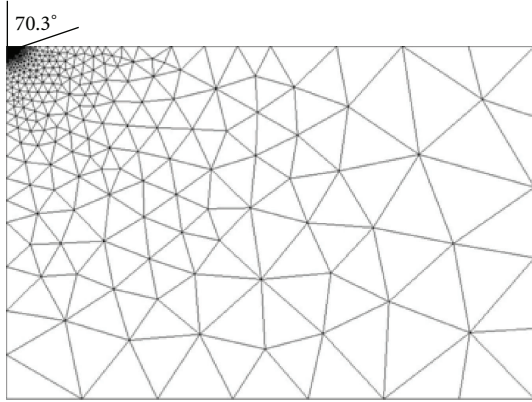


FIGURE 12: FEM model.

stability of the finite element calculations. The elements under the indenter measured less than 10 nm to ensure convergence and to model contact accurately. To avoid edge effects, the total width and height of the mesh were set to 300 and 200 μm , respectively. These values are greater than those of the indent.

To determine the parameter of the FEM model, input is required for the NSSL that is derived from the aforementioned nanoindentation experiment. Elastic modulus and Poisson's ratio are 227 GPa and 0.3, respectively. The indenter was displaced downward at 2500 nm for the simulation of indentation process. This depth is similar to that applied in the nanoindentation experiment. The material in this study is assumed to be isotropic, and its plastic behavior is described by the von Mises yield criterion. The indentation process can be simulated using the finite element mesh, as illustrated in Figure 12.

The numerical simulation begins with modulating the material according to the representative stress obtained using (6). That of the NSSL is 1.1 GPa, as determined by comparing the experimental and numerical loading curves depicted in Figure 13. Antunes et al. [25] proposed a new method for evaluating the strain-hardening exponent using the information in the loading-unloading curve. The materials differed in terms of their unloading curves given various values of strain-hardening exponents and constant Young's modulus and representative stress values. This result indicates the variation in stiffness evaluated at maximum load. The strain-hardening exponent can be determined specifically from the slope of the experimental unloading curve on the basis of the aforementioned analysis. The comparison results of experimental and numerical stiffness suggest that the strain-hardening exponent of the NSSL is 0.06, which is much smaller than that for the matrix ($n = 0.385$). Thus, the plastic behavior of the NSSL and of the matrix can be written as

$$\begin{aligned} \sigma_{\text{NSSL}} &= 1025 \left(1 + 202.9\varepsilon_p\right)^{0.06} \\ \sigma_{\text{Matrix}} &= 0.280 \left(1 + 707.1\varepsilon_p\right)^{0.385}, \end{aligned} \quad (7)$$

where ε_p is the plastic strain. The stress-strain curves of the NSSL and of the matrix are shown in Figure 14. The yielding

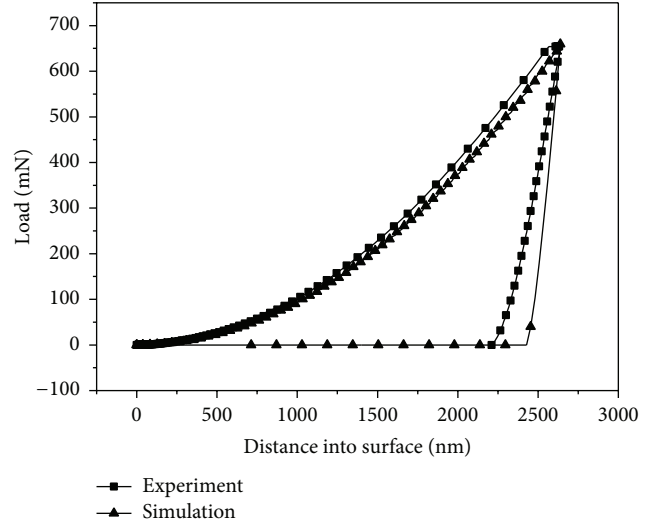


FIGURE 13: Experiment and simulation of load-depth curves.

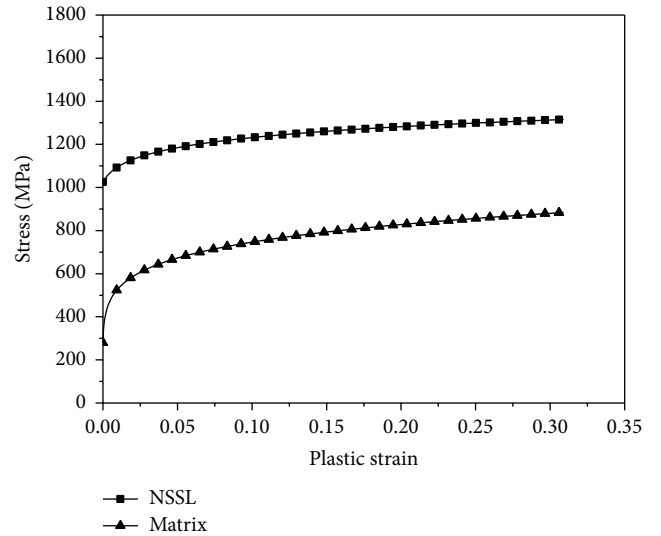


FIGURE 14: Stress-plastic strain curves of the NSSL and of the matrix.

stress of the NSSL is 1025 MPa, which is approximately four times higher than that of the matrix (280 MPa). The high strength of the NSSL is attributed to the nanometer grains and to the martensite induced during SNC.

3. Conclusions

NSSL was generated on a 316L stainless steel plate through SNC treatment. The microstructural and mechanical properties of the NSSL were analyzed through TEM, SEM, nanoindentation, and FEM. The research findings may be summarized as follows:

- (1) TEM results show that the grains in the NSSL measure 8 nm. Moreover, the nanocrystalline grains take the form of random crystallographic orientation and are roughly equiaxed in shape.

- (2) In situ SEM observations of the tensile process confirm that the motions of the dislocations that are determined from within the material are blocked by the NSSL, thereby improving overall yielding stress.
- (3) The nanoindentation test results show that the hardness and the elastic modulus of the NSSL are greater than those of the matrix.
- (4) The yielding strength of the NSSL is approximately 1025 MPa, as per FEM simulation.

Competing Interests

The authors declare that they have no competing interests.

Acknowledgments

The authors are grateful for support from the National Natural Science Foundation of China (nos. 11362013, 11062007, and 11562016), the Research Fund for the Doctoral Program of Higher Education of China (no. 20121514130001), and the Natural Science Foundation of Inner Mongolia Autonomous Region (nos. 2015MS0121 and 2013MS0107).

References

- [1] H. Gleiter, "Nanocrystalline materials," *Progress in Materials Science*, vol. 33, pp. 223–235, 1988.
- [2] K. Lu, "Nanocrystalline metals crystallized from amorphous solids: nanocrystallization, structure, and properties," *Materials Science and Engineering R: Reports*, vol. 16, no. 4, pp. 161–221, 1996.
- [3] K. Lu and J. Lu, "Surface nanocrystallization of metallic materials—presentation of the concept behind a new approach," *Journal of Materials Science and Technology*, vol. 15, no. 3, pp. 193–197, 1999.
- [4] Z. B. Wang, J. Lu, and K. Lu, "Chromizing behaviors of a low carbon steel processed by means of surface mechanical attrition treatment," *Acta Materialia*, vol. 53, no. 7, pp. 2081–2089, 2005.
- [5] N. R. Tao, Z. B. Wang, W. P. Tong, M. L. Sui, J. Lu, and K. Lu, "An investigation of surface nanocrystallization mechanism in Fe induced by surface mechanical attrition treatment," *Acta Materialia*, vol. 50, no. 18, pp. 4603–4616, 2002.
- [6] Y.-J. Mai, X.-H. Jie, L.-L. Liu, N. Yu, and X.-X. Zheng, "Thermal stability of nanocrystalline layers fabricated by surface nanocrystallization," *Applied Surface Science*, vol. 256, no. 7, pp. 1972–1975, 2010.
- [7] D. Li, H. N. Chen, and H. Xu, "The effect of nanostructured surface layer on the fatigue behaviors of a carbon steel," *Applied Surface Science*, vol. 255, no. 6, pp. 3811–3816, 2009.
- [8] G. Liu, S. C. Wang, X. F. Lou, J. Lu, and K. Lu, "Low carbon steel with nanostructured surface layer induced by high-energy shot peening," *Scripta Materialia*, vol. 44, no. 8–9, pp. 1791–1795, 2001.
- [9] N. R. Tao, M. L. Sui, J. Lu, and K. Lu, "Surface nanocrystallization of iron induced by ultrasonic shot peening," *Nanostructured Materials*, vol. 11, no. 4, pp. 433–440, 1999.
- [10] G. Liu, J. Lu, and K. Lu, "Surface nanocrystallization of 316L stainless steel induced by ultrasonic shot peening," *Materials Science and Engineering A*, vol. 286, no. 1, pp. 91–95, 2000.
- [11] X. Wu, N. Tao, Y. Hong, B. Xu, J. Lu, and K. Lu, "Microstructure and evolution of mechanically-induced ultrafine grain in surface layer of AL-alloy subjected to USSP," *Acta Materialia*, vol. 50, no. 8, pp. 2075–2084, 2002.
- [12] B. N. Mordyuk, G. I. Prokopenko, M. A. Vasylyev, and M. O. Iefimov, "Effect of structure evolution induced by ultrasonic peening on the corrosion behavior of AISI-321 stainless steel," *Materials Science and Engineering A*, vol. 458, no. 1–2, pp. 253–261, 2007.
- [13] Y. F. Al-Obaid, "Shot peening mechanics: experimental and theoretical analysis," *Mechanics of Materials*, vol. 19, no. 2–3, pp. 251–260, 1995.
- [14] M. Kobayashi, T. Matsui, and Y. Murakami, "Mechanism of creation of compressive residual stress by shot peening," *International Journal of Fatigue*, vol. 20, no. 5, pp. 351–357, 1998.
- [15] S. A. Meguid, *Mechanics of shot peening [Ph.D. thesis]*, UMIST, Manchester, UK, 1975.
- [16] S. Bagherifard, R. Ghelichi, and M. Guagliano, "A numerical model of severe shot peening (SSP) to predict the generation of a nanostructured surface layer of material," *Surface and Coatings Technology*, vol. 204, no. 24, pp. 4081–4090, 2010.
- [17] H. Y. Miao, S. Larose, C. Perron, and M. Levesque, "An analytical approach to relate shot peening parameters to Almen intensity," *Surface and Coatings Technology*, vol. 205, no. 7, pp. 2055–2066, 2010.
- [18] Y. M. Xing and J. Lu, "An experimental study of residual stress induced by ultrasonic shot peening," *Journal of Materials Processing Technology*, vol. 152, no. 1, pp. 56–61, 2004.
- [19] T. Kim, H. Lee, H. C. Hyun, and S. Jung, "A simple but effective FE model with plastic shot for evaluation of peening residual stress and its experimental validation," *Materials Science and Engineering A*, vol. 528, no. 18, pp. 5945–5954, 2011.
- [20] T. Roland, D. Retraint, K. Lu, and J. Lu, "Enhanced mechanical behavior of a nanocrystallised stainless steel and its thermal stability," *Materials Science and Engineering A*, vol. 445–446, pp. 281–288, 2007.
- [21] W. Yan, L. Fang, Z. Zheng, K. Sun, and Y. Xu, "Effect of surface nanocrystallization on abrasive wear properties in Hadfield steel," *Tribology International*, vol. 42, no. 5, pp. 634–641, 2009.
- [22] Y. Ochi, K. Masaki, T. Matsumura, and T. Sekino, "Effect of shot-peening treatment on high cycle fatigue property of ductile cast iron," *International Journal of Fatigue*, vol. 23, no. 5, pp. 441–448, 2001.
- [23] W. C. Oliver and G. M. Pharr, "Measurement of hardness and elastic modulus by instrumented indentation: advances in understanding and refinements to methodology," *Journal of Materials Research*, vol. 19, no. 1, pp. 3–20, 2004.
- [24] M. Dao, N. Chollacoop, K. J. Van Vliet, T. A. Venkatesh, and S. Suresh, "Computational modeling of the forward and reverse problems in instrumented sharp indentation," *Acta Materialia*, vol. 49, no. 19, pp. 3899–3918, 2001.
- [25] J. M. Antunes, J. V. Fernandes, L. F. Menezes, and B. M. Chapparó, "A new approach for reverse analyses in depth-sensing indentation using numerical simulation," *Acta Materialia*, vol. 55, no. 1, pp. 69–81, 2007.
- [26] W. C. Oliver and G. M. Pharr, "Improved technique for determining hardness and elastic modulus using load and displacement sensing indentation experiments," *Journal of Materials Research*, vol. 7, no. 6, pp. 1564–1580, 1992.
- [27] M. Lichinchi, C. Lenardi, J. Haupt, and R. Vitali, "Simulation of Berkovich nanoindentation experiments on thin films using

finite element method," *Thin Solid Films*, vol. 312, no. 1-2, pp. 240-248, 1998.

- [28] Y. Sun, T. Bell, and S. Zheng, "Finite element analysis of the critical ratio of coating thickness to indentation depth for coating property measurements by nanoindentation," *Thin Solid Films*, vol. 258, no. 1-2, pp. 198-204, 1995.



Hindawi

Submit your manuscripts at
<http://www.hindawi.com>

